Published in final edited form as:
Opt Express. 2007 ; 15(4): 16141–16160. doi:10.1364/OE.15.016141.

In vivo functional imaging of human cone photoreceptors

Ravi S. Jonnal, **Jungtae Rha**[*], **Yan Zhang**[**], **Barry Cense**, **Weihua Gao**, and **Donald T. Miller**
School of Optometry, Indiana University, Bloomington, Indiana 47405

[*]Current affiliation: The Eye Institute, Medical College of Wisconsin, Milwaukee, Wisconsin 53226

[**]Current affiliation: Alcon Laboratories, Inc., Ft. Worth, Texas 76134

Abstract

We evaluate a novel non-invasive optical technique for observing fast physiological processes, in particular phototransduction, in single photoreceptor cells in the living human eye. The method takes advantage of the interference of multiple reflections within the outer segments (OS) of cones. This self-interference phenomenon is highly sensitive to phase changes such as those caused by variations in refractive index and scatter within the photoreceptor cell. A high-speed (192 Hz) flood-illumination retina camera equipped with adaptive optics (AO) is used to observe individual photoreceptors, and to monitor changes in their reflectance in response to visible stimuli ("scintillation"). AO and high frame rates are necessary for resolving individual cones and their fast temporal dynamics, respectively. Scintillation initiates within 5 to 10 ms after the onset of the stimulus flash, lasts 300 to 400 ms, is observed at visible and near-infrared (NIR) wavelengths, and is highly sensitive to the coherence length of the imaging light source. To our knowledge this is the first demonstration of *in vivo* optical imaging of the fast physiological processes that accompany phototransduction in individual photoreceptors.

1. Introduction

Human vision starts when photoreceptors collect and respond to light, a complex biochemical cascade of events referred to as phototransduction. Normal photoreceptor function is essential for normal vision yet is lost when photoreceptors degenerate, which occurs in many blinding diseases including macular degeneration and retinitis pigmentosa. The phototransduction process has been extensively studied *in vitro*, resulting in detailed models of the biochemical cascade (see, for example, [1]). Techniques to assess these processes *in vivo*, however, are limited. This is primarily because current optical and electrophysiological techniques have limited spatial resolution and sensitivity, and target only specific functional processes. Direct observation in the living human eye has been confined to the initial photon absorption kinetics (measured by photopigment densitometry [2]) and the final membrane hyperpolarization (measured by electrophysiology [3,4]). While these techniques have allowed macroscopic investigation of large patches of retina, they have not allowed probing of the function of individual photoreceptors.

An alternative to electrophysiology is NIR optical imaging. Near-IR permits non-invasive probing of scattering changes in retinal tissue without initiating phototransduction itself owing to the insensitivity of photoreceptors at these longer wavelengths. The last 30 years have established light-evoked IR scatter as a key observable in investigating *in vitro* the phototransduction process (especially intermediate stages) in rod photoreceptors (see, for

E-mail: rjonnal@indiana.edu.

example, [5,6,7]). More recently, flood illumination NIR imaging, coupled with dark field and polarization methods, have shown stimulus-evoked scatter in dissected and isolated frog and salamandar retina along with cellular resolution imaging [8]. Conventional imaging techniques used to measure this scatter, however, have not transferred to the living eye where their full impact can be realized. There are several key reasons for this.

First the axial resolution of the conventional techniques is poor. In some cases the depth location of the scatter is inferred by measuring the total scatter from the bulk retina and carefully manipulating the retina's response with invasive physiologic solutions. Second, the instruments were designed for probing the retina in transmission. This works well for isolated retina with the retinal pigment epithelium (RPE) and choroid removed, but is not applicable for the living retina where measurements must be made in reflection. Third, the techniques were not designed for imaging through the intact optics of the eye where the numerical aperture is limited and ocular aberrations blur the scatter signals, reducing sensitivity and specificity of the measurements. Lastly, the instruments were not designed to handle retina motion, which can noticeably blur scatter signals at the cellular scale.

Recent advances in optical coherence tomography (OCT) have successfully overcome the first two problems: poor axial resolution and imaging in reflection. Yao, et al. [9] used a standard resolution (19 μm axial), non-scanning OCT with fixed-depth selection to record a light-evoked fast decrease in the return IR scatter from the photoreceptor layer in an inverted frog retina with RPE removed. Bizheva, et al. [10] employed ultrahigh-resolution OCT (3.5 μm axial) to image isolated rabbit retina (without RPE). In contrast to Yao, et al., they recorded a light-evoked slow (seconds) increase in the OS and a slow (seconds) decrease in the inner segment of the photoreceptors. This technology, however, was not transferred to the living human eye. The instrument's 1.3 μm light source is readily absorbed by ocular tissue and the instrument's slow scan rate of 222 A-scans/s would expose the image to prohibitive eye motion. Srinivasan et al. [11] addressed both limitations by using spectral-domain OCT (SD-OCT) (2.8 μm axial resolution) to measure light-evoked IR scatter in the living rat retina. Images were acquired at a rate of 24,000 A-scans/s and at a wavelength of 890 nm, which readily passes through ocular tissue. Light-evoked IR scatter was found to increase in the OS of rod photoreceptors, consistent with the earlier finding of Bizheva, et al.

While successful, these OCT studies were limited to animal eyes (not human), functional imaging of rods (not cones, which are more critical for human vision and likely have different scatter characteristics), and the collective response of many cells (not individual cells). The last was due to the necessity of averaging A-scans to overcome insufficient sensitivity and image blur caused by the optics of the eye and diffraction. In this paper we propose an alternative imaging approach that aims to overcome these obstacles, permitting the detection of individual cone responses in human subjects. To achieve this, the instrument is based on conventional flood illumination with 192 Hz image acquisition and AO. The high speed permits tracking millisecond scale transient scatter changes and eliminates retina motion artifacts. Such high speed is likely required as ERG studies indicate that the human cone a-wave initiates within a few milliseconds of stimulus onset, and that its time-to-peak is approximately 15 ms [3]. AO permits near-diffraction-limited imaging across a dilated pupil, which enables the resolution of individual cone cells. The camera outperforms SD-OCT in lateral resolution (< 3 μm) and speed (192 fps at 100 MHz pixel rate), both of which may be critical in elucidating characteristics of the light-evoked IR scatter. An important tradeoff is significantly lower axial resolution. Nevertheless, AO flood illumination cameras have been highly successful for studying cone photoreceptors and in particular detecting the waveguided light that exit the cones [12,13,14,15,16]. Since this light traverses the cones, it should be directly impacted by optical changes that occur within these cells.

Light-evoked scatter is weak. To increase signal to noise (SNR), we increased the temporal coherence of the imaging light source such that light scatter along the full extent of the cone OS, including that at the connecting cilia (CC) and posterior tips (PT) of the OS, coherently interferes. As a result, the detected signal is the sum of the complex amplitudes, rather than the sum of the intensities, of reflecting layers. Coherent interference of the scattered light should amplify the signal and make image contrast highly sensitive to small optical changes, much more so than incoherent illumination. For convenience we term this coherent effect “self-interference” as it corresponds to the interference of reflections from within the photoreceptor. Likewise, a stimulus-evoked change in the self-interference is termed “scintillation” as this captures the pronounced oscillatory nature of the cone reflection following a stimulus. Self interference is directly analogous to the coherence effect that is fundamental in optical interferometers and makes these instruments highly sensitive to sub-wavelength changes in optical path length. Similarly, imaging with coherent light has been used to measure blood flow in subsurface capillaries whose weakly reflecting light coherently interfere to produce high contrast speckle [17].

In this paper we validate the flood illumination methodology with which we evoke and observe scintillation in individual cones. We characterize the temporal properties of cone scintillation in terms of its response, duration, frequency, time-RMS, and dependence on wavelength and coherence length of the imaging source. Based on these findings, we propose an optical model of how the retinal reflection contributes to this phenomenon. The most simple explanation attributes it to coherent interference of two bright reflections that axially demarcate the cone outer segment. This simplified model predicts oscillations in reflectance, following stimulus, quite similar to the chirped sinusoidal oscillation observed in the experiments. Comparison of cone scintillation to the general characteristics of electroretinograms (ERGs), which measure changes in voltages, is included. It should be cautioned, however, that while scintillation and ERGs may convey complementary information about physiological processes in the photoreceptors, their appearance may be strikingly different as the two are generated by fundamentally different mechanisms, one optical and the other electrical. In particular, the putative roles of interference and random initial phase in scintillation suggest that initial changes in a cone's reflectance may be positive or negative, which is not the case with ERG signals.

Early accounts of this work were presented at the Optical Society of America meeting in 2004 [18] and the Association for Research in Vision and Ophthalmology (ARVO) meetings in 2005, 2006, and 2007 [19,20,21]. Preliminary results were provided in Fig. 10 of Rha et al. [16] and in [22].

2. Methods

2.1. Apparatus and protocol

2.1.1. Adaptive optics retina camera—A high-speed flood-illumination camera was developed for collecting aerial images of microscopic structures in the living human retina. The camera consisted of four sub-systems: (1) AO for compensation of the eye's wave aberrations, (2) pupil retro-illumination and fixation channel for alignment of the subject's eye to the camera, (3) retinal imaging using one of three fiber-based light sources and two scientific-grade charge-coupled devices (CCDs), and (4) visible stimulus delivery using a fiber-based light source. A schematic of the camera is shown in Fig. 1.

The AO system is described in detail elsewhere [23,16]. In short, the system consists of a Shack-Hartmann wavefront sensor (SHWS) and 37 actuator deformable mirror (Xinȼtics, Inc.) that are controlled in closed loop at 15 Hz via a desktop computer. A 17×17 lenslet array, placed conjugate to the eye's pupil, samples the exiting wavefront across a 6.8 mm pupil. The

deformable mirror is positioned upstream of the lenslet array at a plane conjugate to the eye's pupil. The middle horizontal row of mirror actuators traverses 6.8 mm at the eye's pupil. The power of the 788 nm AO beacon at the cornea was 5.0 μW, approximately 100 times below the ANSI limit [24].

The illumination channel for retinal imaging consists of three light sources, two laser diodes (LD) and a superluminescent diode (SLD). These sources are shown in Table 1 along with their mean wavelengths (λ), spectral bandwidths (Δλ), and coherence lengths inside the cone photoreceptors (L_c). Coherence length was calculated using $L_c = \frac{2\ln 2\ \lambda^2}{n\pi\Delta\lambda}$ where n is the refractive index of the OS and set at 1.43, following Snyder [25]. Each of these sources was coupled to a length of multimode fiber used to reduce the spatial coherence of the light and provide quasi-uniform illumination. Multimode fiber lengths are also given in Table 1. Methods for calculating adequate multimode fiber lengths are given in Rha, et. al [16]. A customized spectral bandpass filter was placed immediately downstream of the 835 nm SLD, allowing the bandwidth and coherence length to be altered, as specified in Table 1. To optimize efficiency, the filter was designed such that its transmission spectrum was centered on the output spectrum of the SLD. As given in Table 1, somewhat different retinal patch sizes were illuminated depending on the experiment and power constraints of the sources. The typical power level entering the eye for each source is also given. When used as a stimulus source, the 670 nm LD delivered up to 169 million Trolands (Td) over pulses ranging from 250 μm to 32 ms. It illuminated a 1.8 degree patch of retina, concentric with the 1.7 degree and 1.0 degree imaging patches.

Two back-illuminated scientific-grade 12 bit CCD cameras (Quantix 57, Ropier Scientific, Inc., and Cam1M100-SFT, Sarnoff Imaging) captured aerial images of the retina, and were synchronized with the light sources and shutters to carefully control light delivery and detection.

The cameras are frame transfer and have light-sensitive arrays of 512×530 (Quantix) and 1000×500 (Sarnoff) pixels. Read noise is 18 e- RMS (Quantix) and 28 e- RMS (Sarnoff). The full-frame acquisition rates for the cameras were 10 Hz (Quantix) and 192 Hz (Sarnoff), using exposure times of 2-4 ms and 5 ms, respectively. The Quantix frame rate was boosted to 30 Hz by reducing the field of view to 256×256 px. Data were collected at 30 Hz (Quantix) and 192 Hz (Sarnoff).

While all of the experiments (described below) could have been conducted using the Sarnoff camera, this camera was unavailable for the last two experiments, which utilized the Quantix. The objectives of the experiments were not compromised by its slower acquisition and actually benefited from the fact that this camera had been rigorously evaluated previously for video-rate imaging of the cone mosaic [16].

2.1.2. Imaging protocol—Cone images were collected on two subjects (33 and 40 years of age) that were free of ocular disease and had normal corrected vision. Spectacle sphere and cylinder, obtained by a professional subjective refraction, ranged from -1.5 to -2.5 diopters and 0.0 to -0.25 diopters, respectively. The eye was stabilized using a bite bar, and was cyclopleged and dilated using two drops of Tropicamide 1% initially and single drops hourly. Drops of phenylephrine HCL 2.5% were applied if additional dilation was necessary.

Defocus and astigmatism were minimized by inserting appropriate trial lenses at the spectacle plane while monitoring the SHWS wavefront error. Residual defocus and astigmatism associated with quantization of spectacle lens power (0.25 D) and higher order aberrations

were corrected with the AO system. Subjects were dark adapted for 20 minutes prior to each measurement.

All cone mosaic videos were acquired during dynamic closed-loop AO correction, with the wavefront error corrected to 0.12 - 0.15 μm RMS.

2.1.3. Background correction and registration of images—After acquisition, cone videos were background corrected (dark-subtracted and flat-fielded), and registered. Generally, background correction of images was found necessary. Lateral eye motion coupled with nonuniformities across the CCD array and the illumination source generate spurious noise that can mask the desired reflectance changes in the retina.

Images acquired using the Sarnoff camera and 915 nm laser were especially prone to two types of CCD artifacts. The long coherence source generated significant interference within the thinned back-illuminated CCD in the camera, which manifested as fringes across the CCD, sometimes termed “etaloning.” The etaloning results in nonuniformities in gain across the CCD. As the eye moves laterally during image acquisition, retinal structures of interest pass from high-gain to low-gain regions of the CCD, resulting in artifactual fluctuations in measured reflectance. The fringes generated by the 915 nm laser were measured to have contrast up to 30%. Since the silicon of the CCD is more transparent at 915 nm than it is at 835 nm or 670 nm, the etaloning was predicted to be less significant at the latter wavelengths; contrast of the fringes at 835nm was measured to be approximately 10%, and negligible at 670 nm.

The transmissivity of the silicon and the multi-panel construction of the Sarnoff CCD contribute to a second significant artifact: differences in gain among the CCD panels, at the interfaces between panels, and where circuitry is mounted on the front of the CCD. These artifacts lead to smaller, high spatial frequency, variations in gain, and in combination with the low spatial frequency etaloning, complicate attempts to filter flat-field images.

A flat-fielding procedure was developed to effectively correct these artifacts. A dark image was generated by averaging 100 images collected with a light trap in place of the eye. The flat-fielding procedure consisted of subtracting the dark image from each acquired image, and dividing the resulting images by a flat field image (“flat”). The flat was computed by averaging the unregistered dark-subtracted images from the video. The motivation for this approach was the presumption that eye motion between images would decorrelate object (i.e. retinal) information from one image to the next. As such, an average of 400 images might give an accurate estimate of the illumination and CCD nonuniformities, unique to the specific retinal imaging conditions, and requiring no *a priori* knowledge of the object (retina) structure. Letting $V(x,y,t)$ be a data cube containing T images from a single video, with spatial coordinates x and y and temporal coordinate t, and letting $D(x,y)$ represent the dark image, the flat F is:

$$F(x,y)=\frac{1}{T}\sum_{t=1}^{T}\left[V(x,y,t)-D(x,y)\right]. \quad (1)$$

Each background-corrected aquired image $\hat{I}(x,y)$ is:

$$\widehat{I}(x,y)=[I(x,y)-D(x,y)]/F(x,y). \quad (2)$$

Image registration employed a suite of image processing tools: oversampling, Fourier-domain lowpass filtering, morphological opening, cross correlation, spline interpolation of cross correlation and subsequent sub-pixel registration. Choice of registration procedure varied

among data sets, depending on, for example, the extent of the scintillation and the amounts of eye motion within and between frames. Finally, registration coordinates were used to align the original background-corrected images, crop a common area, and assemble them into data stacks for quantitative analysis and image and video generation. An excellent discussion of many of these techniques may be found in [26].

2.1.4. Time RMS images—Computing the temporal standard deviation, or time-RMS, gives a direct measure of the amount of scintillation in a video. Letting $\widehat{V}(x,y,t)$ be a data cube containing flat fielded images from one video, with spatial coordinates x and y and temporal coordinate t, a time-RMS image I_r can be defined over the time interval $[t_1, t_2]$, containing T images, as:

$$I_r(x,y)=\left[\frac{1}{T}\sum_{t=t_1}^{t_2}(\widehat{V}(x,y,t)-\frac{1}{T}\sum_{t=t_1}^{t_2}\widehat{V}(x,y,t))^2\right]^{1/2}. \quad (3)$$

Each pixel in the time-RMS image represents the standard deviation of the intensity of a specific (x,y) location in the cone mosaic and over a specific time interval. In other words, the time-RMS image shows which parts of the cone mosaic underwent a reflectance change and which did not.

2.2. Experiment 1: Determine the temporal characteristics of cone scintillation after a single stimulus flash of varying strength

The reflectance of individual cones was measured before and after delivery of a single brief flash of 670 nm light (Fig. 2, top). The imaging illumination was provided by the 915 nm laser diode. Cone photoreceptors have a luminous efficiency below 7×10^{-7} for wavelengths greater than 830 nm. Imaging at NIR wavelengths (e.g. 915 nm) should therefore induce negligible photopigment bleaching, allowing the scattering properties of the cones to be probed without evoking scintillation [27]. Cone videos were acquired at 192 Hz with the Sarnoff camera and consisted of 400 frames that spanned approximately 2 s. The high frame rate and nearly continuous exposure of the Sarnoff required continuous illumination over the 2 s videos, using 3 mW of power entering the eye. This power level is more than 10 times below the ANSI MPE limit for 2 s exposure durations at 915 nm for a 1.7 degree patch of retina [24]. Stimulus flashes were delivered 0.44 seconds after initiation of image acquisition, giving 84 images of the unstimulated cone mosaic and 316 images (1.56 s) of the stimulated retina. The 670 nm laser delivered the stimulus flashes with a retinal illuminance of 169×10^6 Td and pulse durations ranging from 250 μs to 32 ms. The latter correspond to stimulus energies of 4.23×10^4 Td·s to 5.41×10^7 Td·s. Figure 3 shows the percent of photopigment bleached for each stimulus energy level used in experiment 1, for both L- and M-cones. The stimulated patch of retina was located at 2.5 degrees eccentricity, superior to the fovea. At this location the presence of retinal vasculature was minimal, cones were readily visible with the AO retina camera, and their OS length was measured with OCT to be 28 μm (assuming a refractive index of the OS of 1.43). This is noticeably shorter than the coherence length (88 μm) of the 915 nm imaging source. This assured coherent interference of the reflected light along the entire length of the OS, including the two bright reflections that delimit the OS and are believed to originate at the CC and PT [28,29].

As a control, a mask was inserted in the stimulus channel at a plane conjugate to the retina such that only the nasal half of the imaged retina was stimulated with the 670 nm flash (see Fig. 4). Masking half of the stimulus beam allowed direct comparison of stimulated and unstimulated portions of the retina under essentially identical conditions. Delivering the stimulus 0.43 seconds after initiation of the video establishes an additional baseline, corresponding to the

pre-stimulus reflectance of all the cones in the imaged mosaic. Videos were analyzed to characterize cone scintillation.

2.3. Experiment 2: Test dependence of cone scintillation on presence of stimulus and coherence of the imaging source

This experiment further tests two underlying hypotheses in Experiment 1. First, light stimulation of the cones is necessary to evoke a scatter change at NIR wavelengths. Second, increasing the coherence length of the imaging source increases the strength of the scintillation. As a first step at testing these hypotheses, videos of approximately the same patch of retina at 1.25 degree eccentricity were collected from one subject under four experimental conditions: (1) without stimulus and a short coherence length of the imaging source, (2) without stimulus and long coherence length, (3) with stimulus and short coherence length, and (4) with stimulus and long coherence length.

For consistency, the 670 nm stimulus source in Experiment 1 was also used here. One difference was that the 670 nm source provided a train of pulses (rather than a single one) that were interleaved with the CCD exposures (see Fig. 2, middle). We chose a train of pulses as this represented a worst case scenario in which the retina was illuminated almost continuously with stimuli for the full video duration. If scintillation is indeed dependent on the presence of the stimulus, it should more readily manifest itself under this condition as opposed to that with a single flash. Retinal illuminance of the 670 nm stimulus was 5.64×10^7 Td, delivered in 2 ms pulses, giving a stimulus energy of 1.13×10^5 Td·s.

Test of the second hypothesis required adjusting the coherence length of the imaging source. For this we chose two coherence lengths, one longer than the OS of cones and another appreciably shorter. The 915 nm laser diode used in Experiment 1 could have provided the necessary longer coherence length, but not the shorter one. The latter required a spectral bandwidth wider than that of the 915 nm source. Because of this, we resorted to the 835 nm SLD listed in Table 1, which had a wider bandwidth. OCT measurements at the retinal location imaged for this experiment showed the cone OS lengths to be about 37 μm. The native coherence length of the 835 nm SLD in retinal tissue is 11.5 μm, which satisfies the shorter coherence condition, i.e. being considerably shorter than the 37 μm OS. To realize the longer coherence length, a custom spectral bandpass filter (λ = 835 nm, $\Delta\lambda$ = 5 nm) was temporarily inserted in the illumination channel of the SLD. This filter increased the coherence length to 43 μm, which is slightly longer than the OS. While a still longer coherence might have been preferred, a clear trade-off exists between coherence length and available power. With the custom filter, the power level at the eye was 0.25 mW and resulted in somewhat noisy images of the cones, but nevertheless with sufficient SNR for testing the hypotheses. To avoid power differences between the two coherence conditions that might have otherwise influenced the results, a neutral density filter was used for the low coherence measurements and mimicked the overall attenuation of the bandpass filter (22.2% and 22.5% transmission for the spectral and neutral density filters, respectively).

Cone videos were acquired at 30 Hz with the Quantix camera and consisted of 90 frames that spanned approximately 3 s. The Sarnoff camera was unavailable for this experiment, but the slower speed of the Quantix (the primary difference between the two cameras) was more than sufficient for determining whether cone scintillation occurred for each of the four conditions.

2.4. Experiment 3: Test for presence of cone scintillation at visible wavelengths

Experiments 1 and 2 investigate light-evoked scatter of cones at NIR wavelengths (835 nm and 915 nm). This experiment expands the investigation to possible scatter at visible wavelengths (670 nm). To test in the visible, videos of the cone mosaic were collected on two

subjects using the same 670 nm laser diode (L_c=143 μm) to simultaneously stimulate and image the photoreceptor mosaic (see timing diagram in Fig. 2, bottom). Images were acquired at 30 Hz using the Quantix camera with each video consisting of 60 images collected over 2 s. The camera and laser were synchronized such that the laser was pulsed for 2 ms during each 2 ms exposure of the Quantix. Retinal illuminance was 8.46×10^7 Td, giving a stimulus energy of 1.69×10^5 Td·s. Power at the cornea was a factor of 10 lower than the ANSI MPE [24]. Under these conditions, 99% of photopigment in the L-cones is bleached within 730 ms, or within 22 exposures. Field of view (FOV) was 0.8 degrees. Images were collected at a retinal eccentricity of 1.4 degrees. Videos were examined for possible cone scintillation.

3. Results

3.1. Experiment 1: Determine the temporal characteristics of cone scintillation after a single stimulus flash of varying strength

Cone videos (192 Hz) were collected at 915 nm before and after a single brief flash of 670 nm light. A representative video is given in Fig. 5. The video shows a full field image of the cone mosaic, as well as enlarged images of ten unstimulated cones and ten stimulated cones. Each set of ten cones exhibited the highest time-RMS on their respective halves of the video frame. Visual comparison of both the full field video and the enlarged individual cone videos clearly shows that scintillation is confined to the stimulated portion of the retina and occurs only after onset of stimulus. Additional videos acquired (not shown) also revealed the same scintillation properties.

Time-RMS images computed from the cone videos are shown in Fig. 6 (bottom) for four different levels of stimulus. Time-RMS was calculated using Eq. 3 with t_1 and t_2 set to the onset of stimulus and 0.5 s later, respectively. Qualitatively, the time-RMS images reveal RMS differences between the stimulated and unstimulated regions of the retina. Quantitatively, analysis of the time-RMS images shows statistically significant differences between stimulated and unstimulated cones, as shown in the bar plot in Fig. 6 (top). Interestingly, time-RMS images (e.g., Fig. 6) appear similar in spite of large differences in the stimulus strength. Moreover, no statistical correlation was found between scintillation RMS and stimulus strength ($p > 0.1$).

Next, we evaluated the influence of stimulus strength on the temporal characteristics of scintillation, specifically scintillation duration and frequency. Figure 7 shows representative traces of the scintillation response of the same cone for three different stimulus strengths. A representative cone was selected for these plots. While the response with the weakest stimulus ($.04 \times 10^6$Td·s) is difficult to assess as it occurs near the noise threshold, visual assessment of the remaining two suggests a scintillation duration of about 300 to 400 ms. A more quantitative assessment was performed by estimating the endpoint of the scintillation as the time when intensity falls within a range of values assumed to be the post-scintillation noise floor. This approach yielded comparable values. As with mean time-RMS, the scintillation duration appears to be unaffected by the strength of the stimulus. Interestingly, the opposite holds true for the frequency of the scintillation, which depends strongly on stimulus strength. From these plots it is evident that increasing the stimulus strength increases the number of scintillation cycles.

Finally, it was observed in measurements using stronger stimuli that scintillation visibly begins at most 5 to 10 ms after the onset of the stimulus, as shown in Fig. 7 (right). This effect is difficult to detect in the cases of dimmer stimuli, where small initial changes in reflectance may be masked by noise, as seen in Fig. 7 (left).

3.2. Experiment 2: Test dependence of cone scintillation on presence of stimulus and coherence length of the imaging source

Cone videos (30 Hz) were collected at 835 nm on one subject under four conditions that represent the four possible combinations of stimulus (with and without) and coherence length of the imaging source (short and long). The stimulus was at 670 nm and strobed at 30 Hz. The resulting background-corrected and registered cone videos for the four conditions are shown in Fig. 8 (left) as a 2×2 video collage. The videos are cropped to .31 deg and .34 deg in the x- and y-directions. The quality of the cone images is uncharacteristic of that often reported in the literature using similar research-grade AO cameras. The reduced quality stems from a low SNR and the frequent presence of artifactual global and regional intensity fluctuations. The former is caused by the requirements to use the same light source and illumination power in all four videos (see methods for details). The latter are attributed to the background correction and registration of a randomly moving retina that is illuminated with a somewhat Gaussian beam. As expected, these artifacts were found highly correlated with eye motion. While the quality of these videos is poor, it was nevertheless sufficient for determining whether individual cones scintillate under the four conditions, which is the purpose here.

The no stimulus videos (top left and bottom left panels) show local groups of cones (as opposed to individual cones) that fluctuate near the edge of the illumination region, but these are artifacts as described above and not cone scintillation. The two videos in the right column (with stimulus) show scintillation, but the number of cones that do so is considerably different. With the short coherence (11.5 μm), only a few cones scintillate, whereas with the long coherence (43 μm) nearly every one does. Note that scintillation is most evident near the beginning of the video when the cones contain the most unbleached photopigment. For the long coherence case, scintillation in many cones appears to stop after about 1 s. This is consistent with the time duration for which the L-cone photopigment should be fully bleached given the 670 nm illumination levels. Under these conditions, L-cones are predicted to have 99% of their photopigment bleached within 34 exposures, or 1.125 s.

Shown in Fig. 8 (right) are reflectance plots of all the cones (approximately 65 cones) in equivalent subregions of each of the videos. Printed on each plot is the mean time-RMS of the cones in that condition. The condition leading to the highest mean time-RMS (0.035±0.002) is that of long coherence illumination with the stimulus present, which is significantly higher than the other three cases (0.017±0.001, 0.021±0.001, and 0.022±0.001). This finding is corroborated by the visibly large number of scintillating cones in the bottom right panel of the video. The remaining three conditions have significantly lower time-RMS values, suggesting substantially less scintillation. The lack of scintillation is evident in the two panels of the video without stimulus. The condition of short coherence illumination with stimulus present gives a time-RMS marginally higher than the two conditions without stimulus, likely due to the few scintillating cones in the upper right panel of the video.

3.3. Experiment 3: Test for presence of cone scintillation at visible wavelengths

Videos acquired at 30 Hz using a single visible source (670 nm) for simultaneous stimulus and imaging revealed clear scintillation for most of the cones. In this experiment, a baseline control measurement is not possible, since the illumination source used for imaging also stimulates the cones. Contrast of the scintillation was often 15% to 20%. A representative scintillation pattern of one cone and the mean reflectance of many cones in the same frame are shown in Fig. 9 (right). Contrast of the cone is 19.5%. At the top left of the same figure, an average of registered images is shown that reveals the cone mosaic pattern. At the bottom, a time-RMS image of the same video data set is shown. Analysis of the two images reveals significant correlation (r = 0.60), which suggests an overlap between the structure of the cone photoreceptors and the behavior of scintillation.

Under these imaging conditions, L- and M-cone photopigments are predicted to be 99% bleached within 730 ms (22 exposures) and 9.6 s (287 exposures), respectively. For the cone shown in Fig. 9, the large changes in amplitude characteristic of scintillation appear to end approximately where the image mean begins to change. A large fraction of the cones shared this characteristic, but there were many that did not. Perhaps this difference stems from differences in cone properties such as spectral absorption.

In spite of the structural similarities, those cones which reflect more light do not necessarily scintillate more. Specifically, the bright cones in the intensity image are not necessarily the bright cones in the time-RMS image. The cone whose plot is shown, for instance, is bright in the time-RMS image, suggesting that its intensity fluctuated more than other cones, while the average intensity image indicates that it is not one of the brighter cones in the mosaic.

There is also a marked difference between the contrasts of the two images. The contrast of the average intensity image is 0.39, while the contrast of the RMS image is 0.91. This result suggests that in addition to functional imaging, another key application of photoreceptor self-interference may be contrast enhancement of the cone mosaic.

4. Discussion

4.1. Imaging cone function

Three experiments were conducted to (1) test the utility of a high-speed AO flood-illumination camera for cellular retinal imaging and (2) explore the optical behavior of individual cone photoreceptors when exposed to light stimuli. The camera was found to have sufficient spatial resolution, temporal resolution, and sensitivity to detect and track the fast scintillation patterns generated by individual cones when exposed to stimulus.

Experiment 1 investigated cone scintillation before and after a single brief flash of visible light. Cone videos were acquired at 192 Hz and at a wavelength of 915 nm. The coherence length of the 915 nm source was 88 μm and assured self-interference along the full extent of the 28 μm long OS of the cones. We found scintillation absent prior to the flash as well as absent in the control patch of retina that received no stimulus. This confirmed our expectation that 915 nm light does not evoke optical changes in the cones. After the flash, scintillation was consistently present as observed in both the raw cone videos and corresponding time-RMS images.

Interestingly, the scintillation often manifested itself as a noisy, chirped sinusoidal oscillation with faster oscillations at the onset. The time-RMS of the post-stimulus, unmasked cones was significantly higher than that of (1) pre-stimulus, masked, (2) post-stimulus, masked, and (3) pre-stimulus, unmasked cones. The latter represent three separate baselines with consistently similar time-RMS values. When the stimulus strength was high, scintillation occured quickly after its onset, 5 to 10 ms after stimulus. Scintillation lasted roughly 300 to 400 ms. The initiation of the scintillation appears to be in accordance with human cone ERG data [3], supporting the claim that scintillation is linked to cone phototransduction. On the other hand, the 300 to 400 ms duration is noticeably shorter than the 1 - 3 s measured by others with OCT [9,10], with the exception of the 0.5 s interval reported by Srinivasan et al. [11]. Comparison with the OCT studies is nevertheless difficult owing to critical differences in the experiments detailed in the introduction.

The time duration (300 to 400 ms) and time-RMS of the scintillation were independent of the stimulus strength. The amplitude of the scintillation is likely independent as well given the general relation that amplitude of a sinusoid is approximately proportional to the square of the RMS of the same sinusoid. This holds (within ±10%) for RMS calculations over at least ¼ of

a full cycle. The sinusoidal oscillations of the scintillation were well above this. In contrast to these independent parameters, frequency of the scintillation was found dependent. Specifically, an increase in illuminance strength increased the number of scintillation cycles. This could be explained if the scintillation represents (phase-wrapped) interference as, for example, would occur between two bright reflections separated by a medium undergoing a change in optical path length.

Experiment 2 further investigated the impact of stimulus on cone scintillation and also looked at the impact of the coherence length of the imaging source. Four possible combinations of stimulus (present and absent) and coherence length (short and long) were considered. Cone videos were acquired at 30 Hz and at a wavelength of 835 nm. The stimulus was strobed at 30 Hz at 670 nm. The videos acquired with and without (670 nm) stimulus reconfirmed our finding in Experiment 1 that scintillation is a stimulus-evoked phenomenon. That the invisible imaging source (this time 835 nm) alone does not generate scintillation, while the addition of a visible stimulus does, suggests that scintillation depends upon physiological processes in the cones that are spectrally tuned to visible light, such as cone photopigment photoisomerization and subsequent biochemical reactions of phototransduction.

The two coherence lengths (11.5 μm and 43 μm) investigated in experiment 2 strategically straddled the OS length of the cones. In the presence of a visible stimulus, almost every cone scintillated with the longer coherence length, while only a few did with the shorter. One possible source for this dramatic difference may be revealed in B-scans of the retina, such as the one shown in Fig. 10. The B-scan, acquired with AO-OCT, is of the same patch of retina investigated in this experiment. In Fig. 10, many cones have two distinct, bright reflections that demarcate the OS, which are believed to correspond to CC and PT [28]. The distance between these bright reflections is approximately 37 μm in the subject of experiment 2. Since the CC and PT reflections are the dominant waveguided reflections from cones (see, for example, [28,30], they should presumably contribute significantly to scintillation. If so, the 37 μm separation would preclude interference of these two bright reflections with the short coherence source, but not the long one. This prediction is consistent with our experimental findings. The fact that a few cones scintillate with the short coherence length suggests occasional interference between layers in the cone that are separated by less than 11.5 μm. In Fig. 10 a few cones do indeed show additional reflections between CC and PT. Small separations between these additional reflections and either CC or PT could result in strong interference, even under short coherence illumination. In short, experiment 2 revealed that scintillation depends critically on both the presence of a visible stimulus and the coherence length of the imaging source.

Experiments 1 and 2 investigated light-evoked scatter of cones at NIR wavelengths (835 nm and 915 nm). Experiment 3 extended this to visible wavelengths (670 nm), where again scintillation was found. This result was not surprising, but also not presumed, given the tremendous variation in absorption of cones across the visible and NIR and the fact that cones are optimized to capture, not reflect, visible light. Another key finding was the high correlation (r=0.60) between cone position in the averaged image and the maxima in the corresponding time-RMS image. This suggests that scintillation originates with light that passes through cones as opposed to the extracellular space between cones. Similar findings were obtained in Experiment 1 and 2, though the correlation was not quantified.

4.2. Modeling cone scintillation

Our experimental findings on cone scintillation lead to a rather straightforward (albeit overly simplified) model of how the retinal reflection contributes to this phenomena. We hypothesize that the cause for scintillation is interference between light reflected from layers in and near the OS of the cone photoreceptor, coupled with changes in the optical path among these

reflections. Figure 10 depicts a model of the retinal reflection, showing the major reflections that contribute to a flood-illuminated image with focus at the cone mosaic. Using the simplifying assumptions described in the Fig. 10 caption, the flood illuminated image may be expressed as

$$I(t)=I_0+2\left|\Psi_1\right|\left|\Psi_2\right|\cos\left(\frac{2\times\pi}{\lambda}2\Lambda(t)\right). \quad 4$$

In Eq. 4, Ψ_1 and Ψ_2 are the amplitudes of reflected light from CC and PT, respectively, 2Λ is the double-pass optical path separation between CC and PT, and λ is the wavelength of the imaging light source. I_0 is the incoherent sum of all the retinal reflections. A key assumption in this model is that the only relevant optical path length that changes in response to stimulus is that of the OS. This is a reasonable assumption given the time course of scintillation and its confinement to the cone apertures, as reported here.

Eq. 4 highlights the necessity to resolve single cones in order to detect scintillation–in other words, the necessity of AO. The initial phase of the scintillation, which is determined by $\Lambda(t)$, should be highly random from one cone to the next given that OS lengths are likely not uniform to within a small fraction of a micron. As such, averaging scintillation over multiple cones will diminish the second term in Eq. 4 and in the limit will approach zero. This leaves behind only the incoherent term I_0, which contains no scintillation information. The result of averaging is easy to appreciate in Fig. 9, where the reflectance of a single cone (solid blue) shows clear scintillation while the average across the image (dashed black) shows no scintillation. This may be in part why scintillation has not been reported in prior studies of light-evoked scatter in photoreceptors.

The double-pass optical path length ($2\Lambda = 2nL$) through the OS is the product of refractive index (n) and physical length (L). Light-evoked biological activity that alters either n or L will therefore directly impact the scintillation pattern as defined by Eq. 4. The optical path length needs only to change by the imaging wavelength (< 1 μm) to produce a full 2 π cycle in the scintillation. For a more complete explanatory model, a mathematical expression is required for Δ, or specifically n or L, that relates optical changes in the OS to light-evoked biological activity. The origin of these optical changes remains uncertain, however, several possible explanations have been considered:

1. *Scattering*. It has been established that stimulation of isolated frog, toad, and cow retinas leads to changes in scattering properties of the retina [5,6,7], and the time scale of these changes, as well as recent OCT results [10] strongly suggest that these changes largely originate in the OS of rod photoreceptors. Indeed, similar scattering effects have been observed in suspensions of rod OS components such as phosophlipids, lipoproteins, G-proteins [31]. Analysis of such results show that the activation of the peripheral disc membrane protein phosphodiesterase (PDE*/transducin) may be the underlying cause for light-evoked scatter [32]. Such changes could effectively alter the contribution of Ψ_{os}, shown in Fig. 10, which would alter the sum of complex amplitudes which constitutes the scintillation signal. A more complex model would be required to account for this condition, and one which would violate the simplifying assumptions used in Eq. 4. However, with the presence of scintillation depending so starkly upon the coherence length of the illumination source, it seems unlikely that an increased contribution of Ψ_{os}, which would in principle interfere with Ψ_1 and Ψ_2 when illuminated with a short coherence source, is the underlying mechanism.

2. *Swelling*. It has also been suggested that physical changes in the sizes of photoreceptor cells, namely cell swelling or shrinking, may accompany the membrane hyperpolarization phase of the visual transduction cascade, as stimulus-evoked osmotic gradients cause rapid influx and eflux of water [9,10]. Such changes in cell volume may be accompanied by changes in L in Eq. 4.

3. *Refractive index*. It is well known that changes in concentration of biomolecules can alter the refractive indices of suspensions. The cascade of biochemical reactions following stimulation of the photoreceptor may lead to changes in refractive index n and subsequent changes in the OPL Λ [33,34]. It is possible that some of the biochemical processes thought to underly the light-evoked scatter may too influence the refractive index of the OS.

Analysis of the scintillation signals suggests that the change in Λ underlying scintillation may be nonlinear, i.e. the oscillations in reflectance often appear to have varying frequencies. If this finding is confirmed, it would suggest that scintillation is not directly due to changes in concentration of activated opsin, activated G-protein, or phosphodiesterase, since these are known to change linearly in response to stimulation [35], regardless of whether the scintillation effect is mediated by scattering or refractive index. It is also clear that scintillation is not due to changes in photopigment concentrations, although these are known to be exponential in nature. Photopigment activation of the rhodopsin molecule is completed in well under one millisecond [36], which is much shorter than the 300 to 400 ms over which scintillation was observed. Photopigment regeneration is too slow (minutes) to account for the relatively large and rapid changes in Λ associated with scintillation. Leading candidates for the underlying cause of scintillation are nonlinear processes taking place within the cone photoreceptor immediately following stimulation, e.g. changes in the concentration of cG, hyperpolarization or other changes in the properties of the OS membrane, or changes in the physical size of the OS due to cell swelling. Obviously, further investigation is needed to formulate a mathematical expression for Λ that links optical changes in the OS to light-evoked biological activity.

5. Conclusion

A novel high-speed AO flood-illumination camera was investigated as a new tool for studying, *in vivo*, the functionality of individual cone photoreceptors based on their reflectance signatures. Three experiments were conducted whose collective results demonstrated that the camera has sufficient spatial resolution, temporal resolution, and sensitivity to detect and track the fast light-evoked scintillation patterns of individual cones. Cone scintillation was characterized in terms of its response, duration, frequency of oscillation, time-RMS, and dependence on wavelength and coherence length of the imaging source. An optical model of the retina was proposed to explain the observed scintillation. The biological activity responsible for creating optical path length changes in the OS and necessary for scintillation to occur requires further investigation.

Acknowledgement

The authors wish to thank the staff of Daniel Jackson and William Monette for machining and electronics support, and Stephen Burns for use of the 835 nm SLD. Financial support was provided by the National Eye Institute grants 1R01EY018339 and 5R01 EY014743. This work was also supported in part by the National Science Foundation Science and Technology Center for Adaptive Optics, managed by the University of California at Santa Cruz under cooperative agreement No. AST-9876783.

References and links

1. Rodiek, RW. The First Steps in Seeing. Sinaur Associates, P.O. Box 407, Sunderland; Massachusetts: 1998. p. 01375-0407.

2. Elsner AE, Burns SA, Webb RH. Mapping cone photopigment optical density. J. Opt. Soc. Am. A 1993;10:52–8. [PubMed: 8478745]
3. Hood DC, Birch DG. Phototransduction in human cones measured using the a-wave of the ERG. Vision Res 1995;35:2801–2810. [PubMed: 8533321]
4. Friedburg C, Allen CP, Mason PJ, Lamb TD. Contributions of cone photoreceptors and post-receptoral mechanisms to the human photopic electroretinogram. J. Physiol 2004;556:819–834. [PubMed: 14990682]
5. Hofmann KP, Uhl R, Hoffmann W, Kreutz W. Measurements of fast light-induced light-scattering and -absorption changes in outer segments of vertebrate light sensitive rod cells. Biophys. Struc. Mech 1976;2:61–77.
6. Harary HH, Brown JE, Pinto LH. Rapid light-induced changes in near infrared transmission of rods in Bufo marinus. Science 1978;202:1083–1085. [PubMed: 102035]
7. Pepperberg DR, Kahlert M, Krause A, Hofmann KP. Photic Modulation of a Highly Sensitive, Near-Infrared Light-Scattering Signal Recorded from Intact Retinal Photoreceptors. Proc. Natl. Acad. Sci. USA 1988;85:5531–5535. [PubMed: 3399504]
8. Yao X-C, George JS. Near-infrared imaging of fast intrinsic optical responses in visible light-activated amphibian retina. J. Biomed. Opt 2006;11
9. Yao X-C, Yamauchi A, Perry B, George JS. Rapid optical coherence tomography and recording functional scattering changes from activated frog retina. Appl. Opt 2005;44:2019–2023. [PubMed: 15835350]
10. Bizheva K, Pflug R, Hermann B, Považay B, Sattmann H, Qiu P, Anger E, Reitsamer H, Popov S, Taylor JR, Unterhuber A, Ahnelt P, Drexler W. Optophysiology: Depth-resolved probing of retinal physiology with functional ultrahigh-resolution optical coherence tomography. Proc. Natl. Acad. Sci. USA 2006;103:5066–5071. [PubMed: 16551749]
11. Srinivasan VJ, Wojtkowski M, Fujimoto JG, Duker JS. In vivo measurement of retinal physiology with high-speed ultrahigh-resolution optical coherence tomography. Opt. Lett 2006;31:2308–2310. [PubMed: 16832468]
12. Liang J, Williams DR, Miller DT. Supernormal vision and high-resolution retinal imaging through adaptive optics. J. Opt. Soc. Am. A 1997;14:2884–2892.
13. Roorda A, Williams DR. Optical fiber properties of individual human cones. J. Vision 2002;2:404–412.
14. Pallikaris A, Williams DR, Hofer H. The reflectance of single cones in the living human eye. Invest. Ophthalmol. Visual Sci 2003;44:4580–4592. [PubMed: 14507907]
15. Choi SS, Doble N, Hardy JL, Jones SM, Keltner JL, Olivier SS, Werner JS. In vivo imaging of the photoreceptor mosaic in retinal dystrophies and correlations with visual function. Invest. Ophthalmol. Visual Sci 2006;47:2080–2092. [PubMed: 16639019]
16. Rha J, Thorn KE, Jonnal RS, Qu J, Zhang Y, Miller DT. Adaptive optics flood-illumination camera for high speed retinal imaging. Opt. Express 2006;14:4552–4569. [PubMed: 19516608]
17. Dunn A, Bolay H, Moskowitz M, Boas D. Dynamic imaging of cerebral blood flow using laser speckle. J. Cereb. Blood Flow Metab 2001;21:195–201. [PubMed: 11295873]
18. Rha, J.; Jonnal, RS.; Zhang, Y.; Miller, DT. Video rate imaging with a conventional flood illuminated adaptive optics retina camera; 88th Optical Society of America Anual Meeting (2004); Conference presentation.
19. Rha J, Jonnal RS, Zhang Y, Miller DT. Rapid Fluctuation in the Reflectance of Single Cones and Its Dependence on Photopigment Bleaching. Invest. Ophthalmol. Visual Sci 2005;46E-abstract 3546
20. Rha J, Jonnal RS, Zhang Y, Cense B, Gao W, Miller DT. Dependence of cone scintillation on photopigment bleaching and coherence length of the imaging light source. Invest. Ophthalmol. Visual Sci 2006;47E-abstract 2666
21. Jonnal RS, Rha J, Zhang Y, Cense B, Gao W, Miller DT. Functional imaging of single cone photoreceptors using an adaptive optics flood illumination camera. Invest. Ophthalmol. Visual Sci 2007;48E-Abstract: 1955
22. Jonnal, RS.; Rha, J.; Zhang, Y.; Cense, B.; Miller, DT. High-speed adaptive optics functional imaging of cone photoreceptors at a 100 MHz pixel rate. In: Manns, F.; Soederberg, PG.; Ho, A.; Stuck, BE.; Belkin, M., editors. Ophthalmic Technologies XVII. SPIE: 2007.

23. Zhang Y, Rha J, Jonnal RS, Miller DT. Adaptive optics parallel spectral domain optical coherence tomography for imaging the living retina. Opt. Express 2005;13:4792–4811. [PubMed: 19495398]
24. ANSI. American National Standard for the Safe Use of Lasers. Vol. Z136.1. Laser Institute of America: 2000.
25. Snyder A. Stiles-crawford effect-explanation and consequences. Vision Res 1972;13:1115–1137. [PubMed: 4713922]
26. Brown LG. A survey of image registration techniques. ACM Comput. Surv 1992;24:325–376.
27. Sharpe LT, Stockman A, Jagla W, Jägle H. A luminous efficiency function, *V* *λ, for daylight adaptation. J. Vision 2005;5:948–968.
28. Zhang Y, Cense B, Rha J, Jonnal RS, Gao W, Zawadzki RJ, Werner JS, Jones S, Olivier S, Miller DT. High-speed volumetric imaging of cone photoreceptors with adaptive optics spectral-domain optical coherence tomography. Opt. Express 2006;14:4380–4394. [PubMed: 19096730]
29. Drexler W, Sattmann H, Hermann B, Ko T, Stur M, Unterhuber A, Scholda C, Findl O, Wirtitsch M, Fujimoto J, Fercher A. Enhanced visualization of macular pathology with the use of ultrahigh-resolution optical coherence tomography. Arch. Ophthalmol.-Chic 2003;121:695–706.
30. Gao W, Cense B, Zhang Y, Jonnal RS, Miller DT. Measuring retinal contributions to the optical Stiles-Crawford effect with optical coherence tomography. Opt. Express. 2007Submitted
31. Kühn H, Bennett N, Michel-Villaz M, Chabre M. Interactions between photoscited rhodopsin and GTP-binding protein: kinetic and stoichiometric analyses from light-scattering changes. Proc. Natl. Acad. Sci. USA 1981;78:6873–6877. [PubMed: 6273893]
32. Arshavsky VY, Lamb TD, Edward J, Pugh N. G proteins and phototransduction. Annu. Rev. Physiol 2002;64:153–187. [PubMed: 11826267]
33. Enoch J, Scandrett J, T. FL Jr. A study of the effects of bleaching on the width and index of refraction of frog rod outer segments. Vision Res 1973;13:171–183. [PubMed: 4681984]
34. Enoch J, Hudson DK, Lakshminarayanan V, Scandrett J, Bernstein M. Effect of bleaching on the width and index of refraction of goldfish rod and cone outer segment fragments. Optometry Vision Sci 1990;67:600–605.
35. Pugh JEN, Lamb TD. Amplification and kinetics of the activation steps in phototransduction. Biochim. Biophys. Acta 1993;1141:111–149. [PubMed: 8382952]
36. Menon ST, Han M, Sakmar TP. Rhodopsin: structural basis of molecular physiology. Physiol. Rev 2001;81:1659–1688. [PubMed: 11581499]

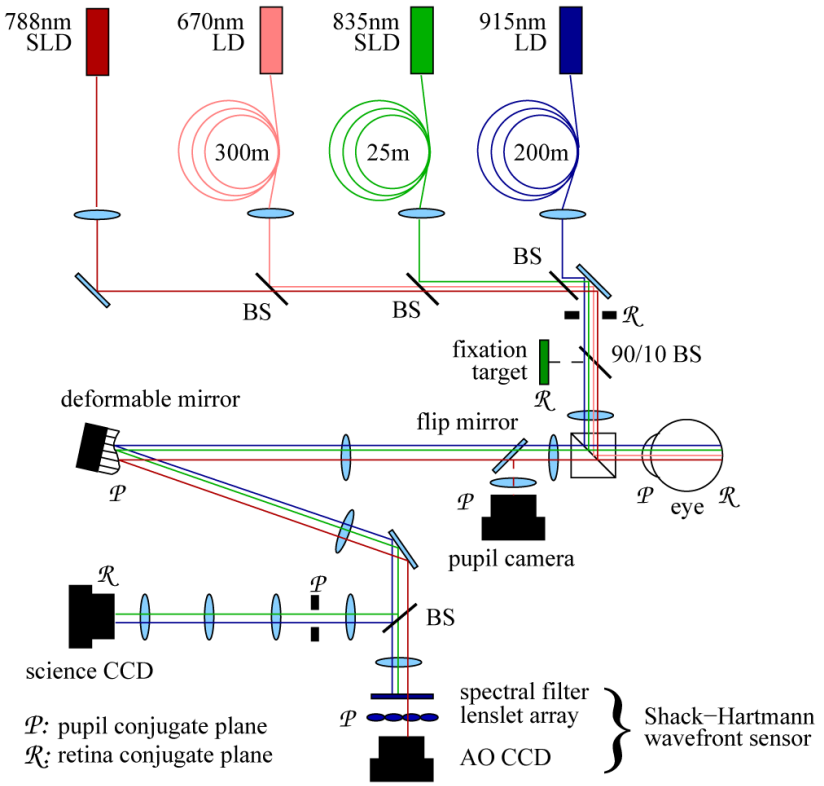

Fig. 1.

Layout of the AO retina camera. The camera consists of four subsystems, described in the text. Custom dielectric beamsplitters were designed to reflect and transmit the various light sources, allowing simultaneous retinal imaging, wavefront correction, and stimulation without loss or mixing of light.

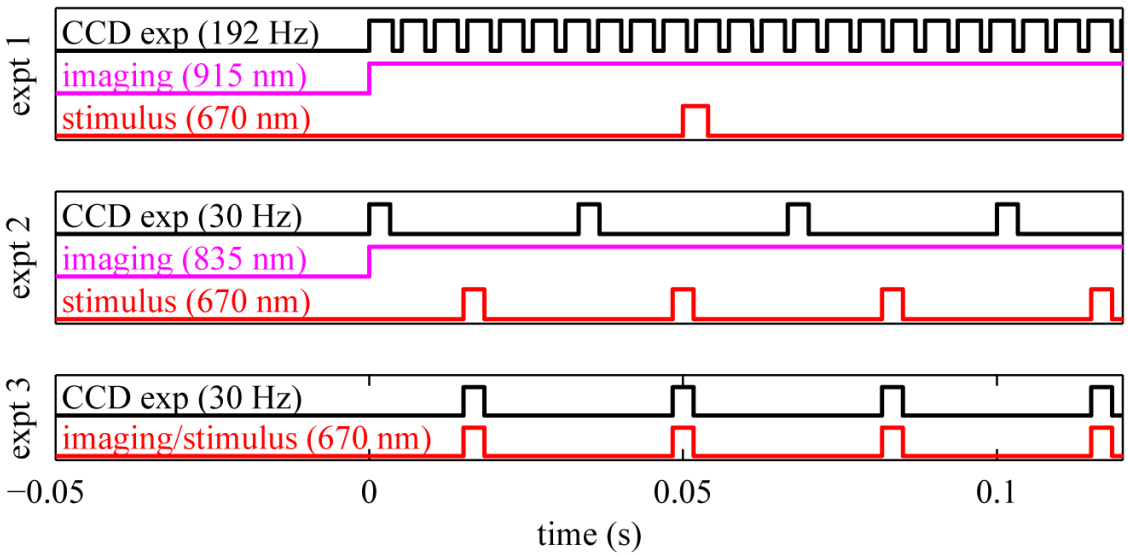

Fig. 2.

Timing diagrams for the experiments. The diagram for experiment 1 (top) shows a single visible stimulus pulse, CW near-infrared illumination for imaging, and the high-speed camera exposures. Experiment 2 (middle) shows CW near-infrared illumination for imaging along with interleaved stimulus pulses and camera exposures. Experiment 3 (bottom) shows a single visible source used as stimulus and illumination, synchronized with camera exposures.

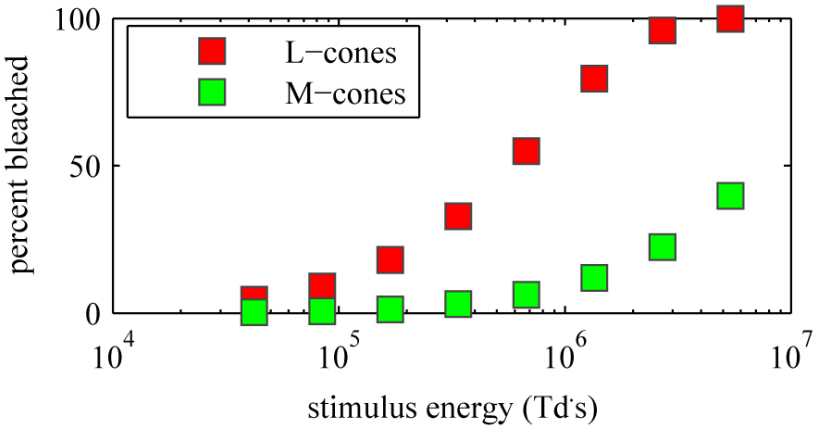

Fig. 3.
(Experiment 1) Predicted bleaching percentages for stimulus energies used.

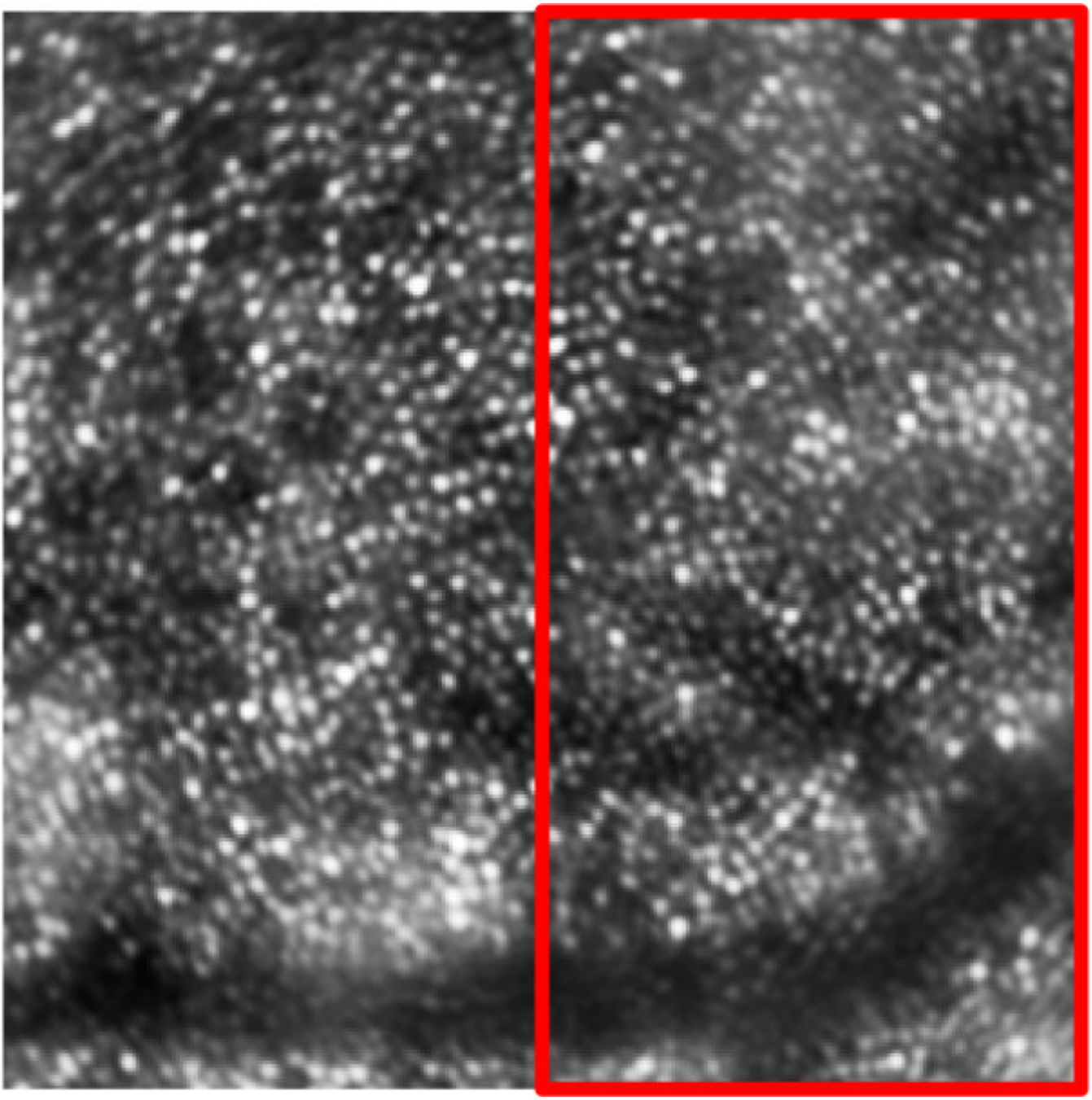

Fig. 4.

(Experiment 1) The imaged retinal patch, along with a schematic depiction of the location of stimulus, designated by a red box. Stimulus was delivered to the right (nasal) portion of the patch shown. Image subtends one degree.

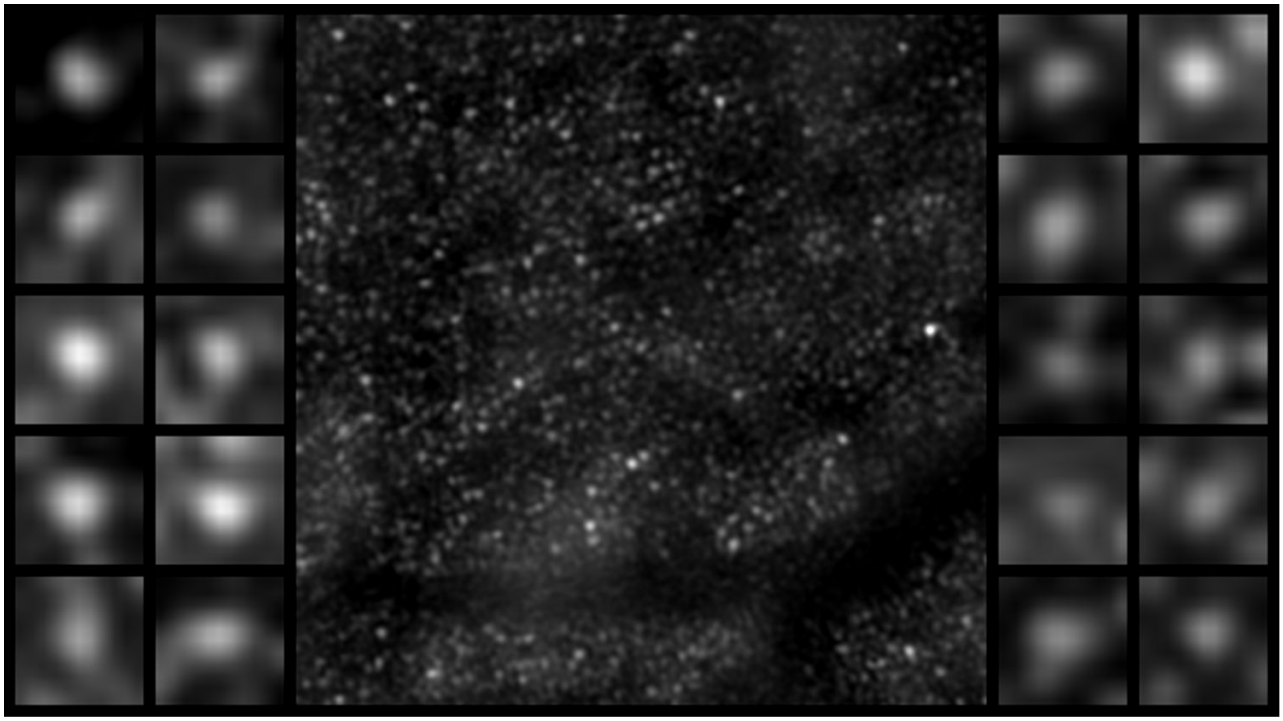

Fig. 5.

(Experiment 1) Representative video showing cone scintillation after a single brief stimulus of 8 ms (or 1:35 × 10^6Td·s). Center panel shows a registered cone mosaic video of 90 frames (.45 s), with 20 frames before stimulus and 70 frames after stimulus. Delivery of stimulus flash to the right half of the patch (see Fig. 4) is depicted by a white flash in the background of the right half of the video. Left panel displays ten cones with highest time-RMS from the unstimulated left half of the video. Right panel shows ten cones with the highest time-RMS in the stimulated right half. The center panel shows cone scintillation is present after the flash in the stimulated half and largely absent in the unstimulated half. The objective selection of the highest time-RMS cones (left and right panels) further highlights this difference. Note that some of the scintillating cones become brighter initially, and others become darker, which supports the hypothesis that interference, with random initial phase, may underlie the phenomenon of scintillation. (AVI video, figure_05.avi, 2.9 MBytes).

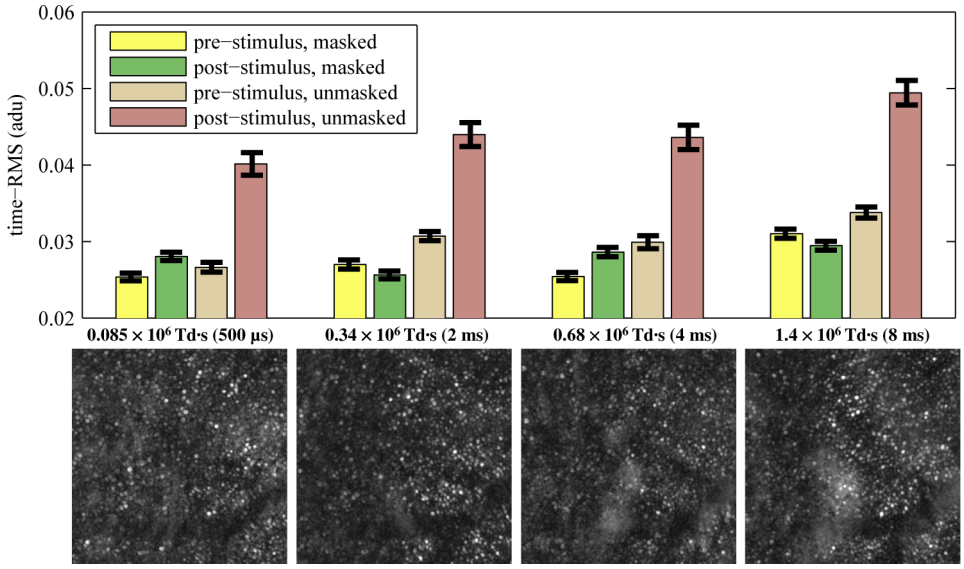

Fig. 6.

(Experiment 1) (bottom) Time-RMS images of the cone mosaic videos for four stimulus levels. Stimulus delivered to the right half (approximately) of each image. Left half was unstimulated. For all stimulus levels, a difference in time-RMS between stimulated and unstimulated retina is evident in the larger number of bright cones in the right half of each time-RMS image. (top) Average time-RMS of cones is shown in the bar graph; error bars show ± one standard error. For each stimulus condition, subregions of the video known to lie in the unstimulated (left) portion of the patch and stimulated (right) portion of the patch were chosen. The subregions were of equal size and equal dimensions. All of the cones in each subregion (about 100 cones each) were analyzed, and their time-RMS values averaged. For each stimulus condition, mean time-RMS is shown for four cases: pre-stimulus, masked; post-stimulus, masked; pre-stimulus, unmasked; and post-stimulus unmasked. The first three cases provide control conditions, showing baseline time-RMS of unstimulated cones. The last shows the experimental condition, showing time-RMS of stimulated cones. Under all four stimulus conditions, the time-RMS of stimulated cones is significantly higher than the time-RMS of control cones.

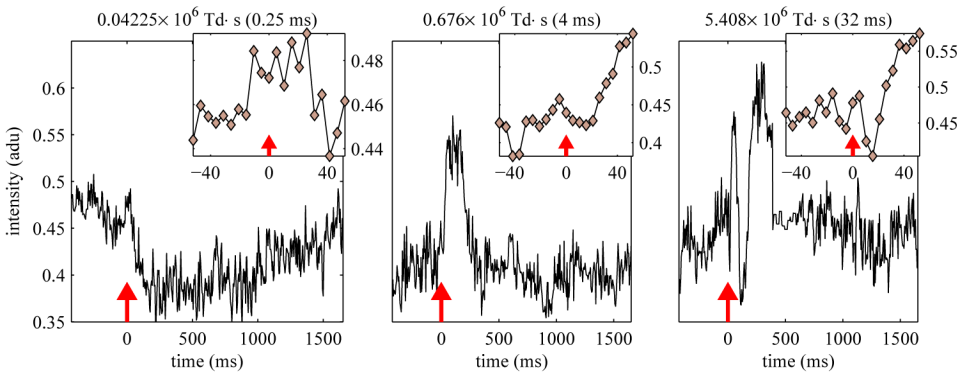

Fig. 7.

(Experiment 1) Reflectance of the same cone before and after a single flash of 670 nm light of varying strength. Stimulus level is shown on each plot in units of Td·s, as well as the corresponding stimulus duration in ms. A red line marks the onset of the stimulus flash. The amplitude of the scintillation is shown as a proportion of the flat field, see § 2.1.3. The variation in initial direction of scintillation supports the hypothesis that interference, with random initial phase, underlies the scintillation phenomenon. The inset of each plot shows a magnified view of the cone's reflectance just before and after stimulation. In the brightest stimulus case (right), it is evident that scintillation begins 5 - 10 ms after stimulus.

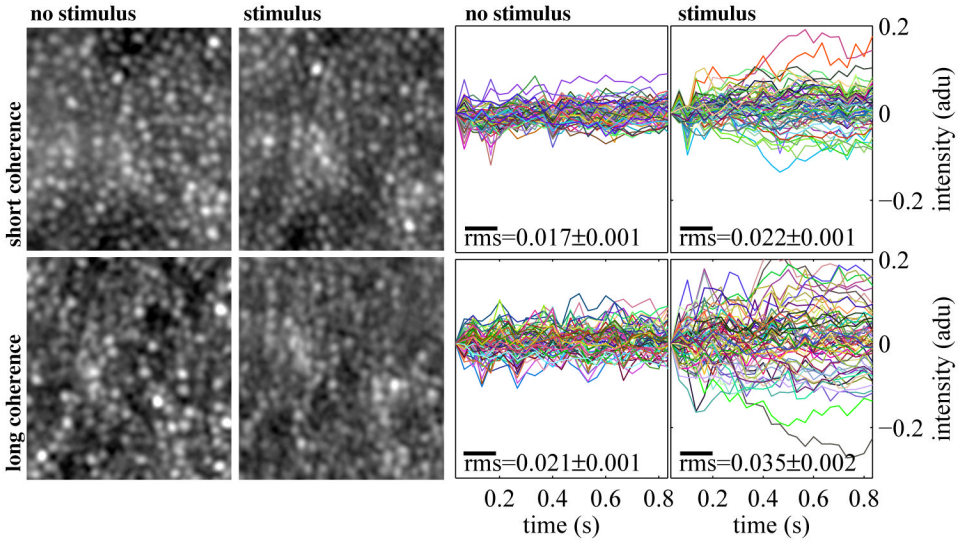

Fig. 8.

(Experiment 2) (left) Cone videos (30 Hz) of the same retinal patch under four different imaging conditions: short coherence and no stimulus (upper left), short coherence and stimulus (upper right), long coherence and no stimulus (lower left), and long coherence and stimulus (lower right). The long coherence/stimulus video shows the most scintillation–nearly every cone scintillates. A few cones appear to scintillate in the short coherence/stimulus case. The videos are .3 degrees in each dimension. (AVI video, figure_08.avi, 0.95 MBytes). (right) Reflectance plots of all of the cones (approx. 65 cones) in subregions of each video. Each cone's reflectance is normalized to its initial reflectance. Shown on each plot is the mean time-RMS of the cones in that condition. Cones in the stimulus/long coherence condition have a mean time-RMS significantly higher than those in the other cases, and this is evident from the reflectance plots as well–the reflectances of these cones appear to spread out over time, owing to their random initial and final phases. Cones in the stimulus/short coherence condition have a mean time-RMS marginally higher than those in either unstimulated case.

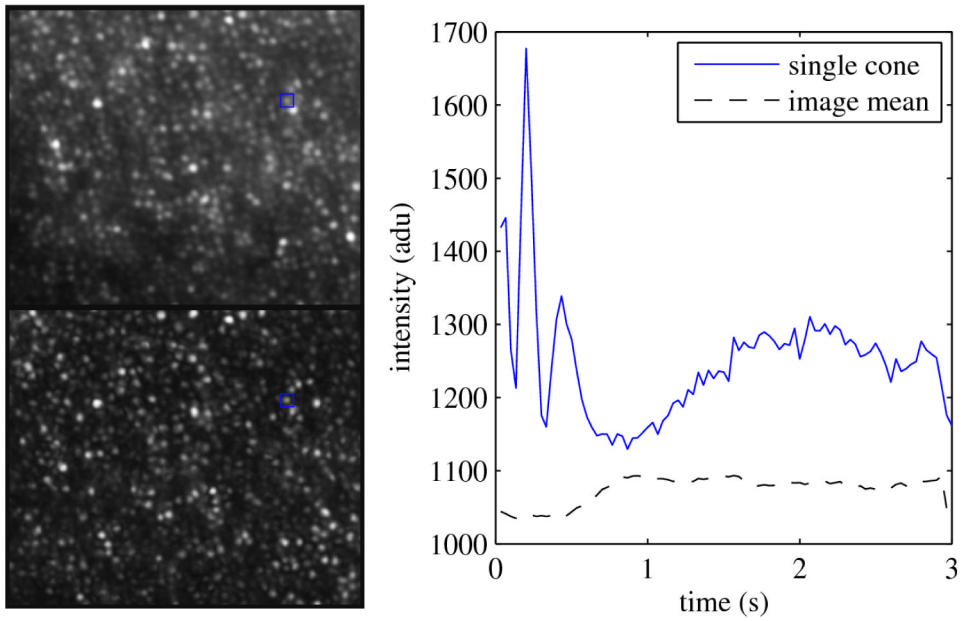

Fig. 9.

(Experiment 3) Cone imaging results using the same 670 nm laser diode (L_c=144 μm) to stimulate and image the retina over a 3 s duration. The top left image represents the registering and co-adding of 90 images acquired at 30 Hz of the same patch of retina. The bottom left image is the time-RMS across the same data set. The right plot traces the scintillation of a single cone (solid blue line) whose location in the cone mosaic (left) is indicated by the blue boxes. Also shown is the average intensity of the entire image (dashed line).

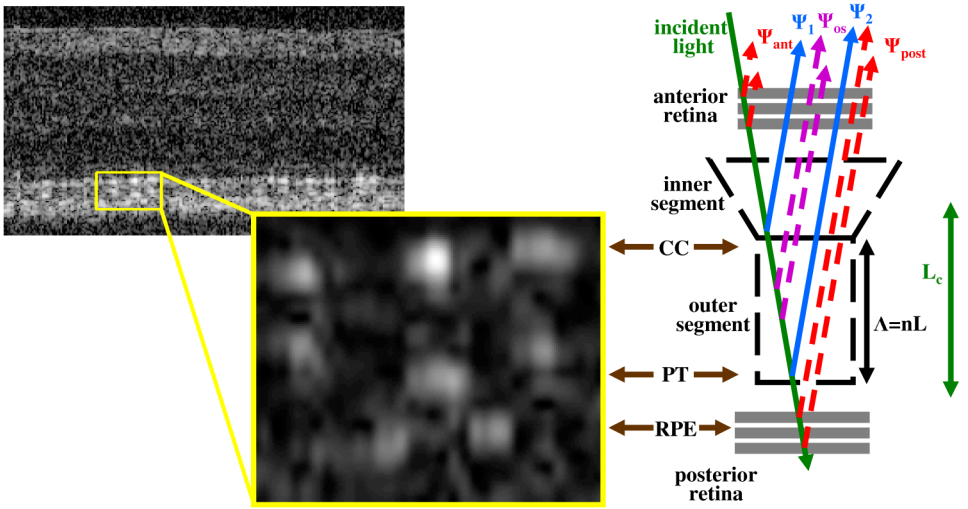

Fig. 10.

(left) AO-OCT B-scan shows spatially-resolved bright reflections at the CC, PT and RPE (defined in text). The nerve fiber layer, a bright band across the top of the B-scan, is shown for reference. (center) An enlarged view of the major reflective layers, displayed in linear scale, is also shown. A regular pattern of bright reflections is evident in the CC and PT layers, with each reflection corresponding to an individual cone photoreceptor [28]. The length of the OS can be measured directly from the B-scans. While most cones have only two bright reflections, at CC and PT, a few have additional reflections inside the OS. The image was collected at 2 degree eccentricity from one of the participating subjects. (right) A model of the retinal reflection depicting potential sources of self-interference is shown. The aerial retinal image with focus at cones, such as those described in experiments 1, 2, and 3, is a complex sum of reflections over much of the retina's depth. However, simplifying assumptions can be made if a visible stimulus is presumed to change only the optical path length of the OS ($\Lambda = nL$) and the coherence length of the imaging source (L_c) is slightly larger than Λ. These assumptions result in Eq. 4. See text for details.

Table 1

Specifications for the various light sources used for illumination and stimulus. The specifications of the SLD without the bandpass filter are indicated by

type	λ (nm)	Δλ (nm)	L_c (μm)	fiber (m)	patch (deg)	power at eye (mW)
LD	670	0.97	144	300	1.8	6.0, 2.0, 3.0 *
SLD	835	18.7†/5.0‡	11.5†/43.0‡	25	1.0	0.250
LD	915	3	88	400	1.7	3.0

† and with the bandpass filter with

‡ Specifications are defined in the text.

* Three different power levels were used in experiments 1, 2, and 3, respectively.